

Properties and applications of quantum dot heterostructures grown by molecular beam epitaxy

M. Henini

Published online: 26 July 2006
© to the authors 2006

Abstract One of the main directions of contemporary semiconductor physics is the production and study of structures with a dimension less than two: quantum wires and quantum dots, in order to realize novel devices that make use of low-dimensional confinement effects. One of the promising fabrication methods is to use self-organized three-dimensional (3D) structures, such as 3D coherent islands, which are often formed during the initial stage of heteroepitaxial growth in lattice-mismatched systems. This article is intended to convey the flavour of the subject by focussing on the structural, optical and electronic properties and device applications of self-assembled quantum dots and to give an elementary introduction to some of the essential characteristics.

Keywords Heterostructures · Semiconductors · Self-assembly · Quantum dots · Lasers · Optoelectronics

Introduction

It is well known that quantum confinement of charge carriers arises from a potential well in the band edges when the well width (typically a few hundred Ångströms) is comparable to the de Broglie wavelength of the carriers. The decreased dimensionality of the free-carrier motion (i.e. confinement) results in the density of states (DOS) of the carriers being modified. The DOS gives a measure of the maximum number of

carriers that can occupy an energy range. The DOS, due to carrier motion in the x , y and z directions of the active region in a double heterostructure (DH) laser, is schematically shown in Fig. 1(a). It can be seen that for a given band (conduction band [CB] or valence band [VB]), the DOS is small near the edge of the band and increases with increasing energy. By reducing the active layer thickness to the order of the de Broglie wavelength (Fig. 1(b)) a two-dimensional quantum well (QW) heterostructure laser is realized. The corresponding DOS, due to confined carrier motion in the z -direction has a step-like shape offering an improvement over DH lasers. In the QW laser the number of electrons and holes populating the CB and VB is largest near the edges. Furthermore, the energy of the optical transition (i.e. frequency of the output light) can be controlled by the well thickness. The discretisation of the energy levels also means that optical transitions will be sharper (i.e. sharp line in the laser output frequency). As a result, these quantum-size effects significantly reduce the threshold current density and its temperature dependence, and shorten the emission wavelength.

One can further limit the motion of the carriers in the y -direction—quantum wire (QWi) laser (Fig. 1(c)) (carriers are confined in two directions) and x -direction—quantum box (QB) laser (Fig. 1(d)) (carriers are free to move in zero dimension, i.e. carriers are confined in three directions). The shape of the DOS in QWi and QB lasers is further improved compared to QW lasers. It has an infinite value near the edges of the bands for the QWi lasers whereas in the QB lasers, carriers occupy discrete levels. The QWi lasers are expected to resemble the spectral linewidth of gas and solid-state lasers more than the conventional DH and QW lasers. This is due to the close resemblance of their

M. Henini (✉)
School of Physics and Astronomy, University
of Nottingham, Nottingham NG7 2RD, UK
e-mail: Mohamed.Henini@Nottingham.ac.uk

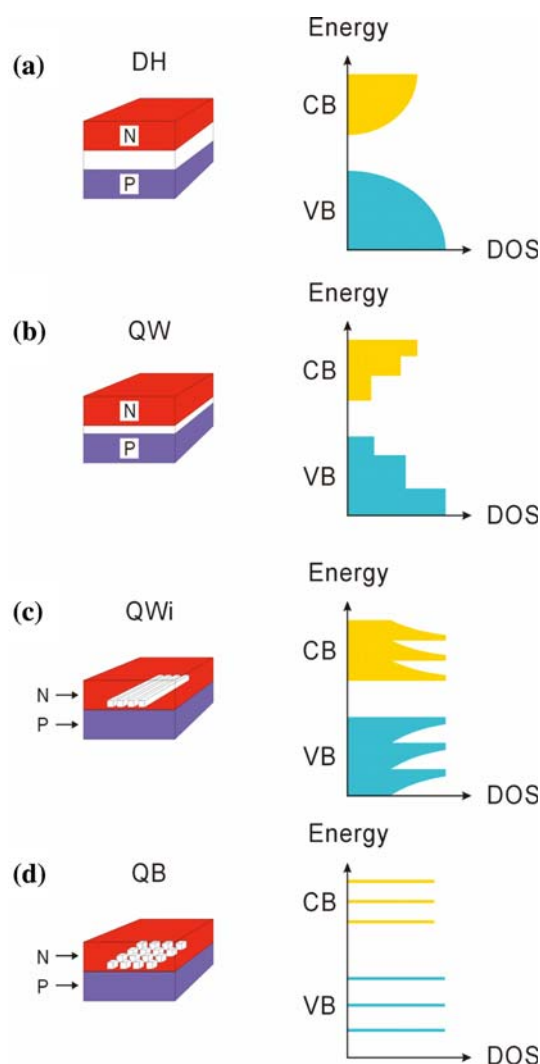


Fig. 1 Schematic diagram of the density of states (DOS) in the conduction band (CB) and valence band (VB) for a (a) double heterostructure, (b) quantum well, (c) quantum wire, and (d) quantum box laser

DOS functions. However, the QB laser should behave similarly to conventional gas and solid-state lasers because the DOS function of QB lasers is truly discrete.

Self assembled quantum dots (QDs) have generated a great deal of scientific and technological interest, exhibiting the effects of zero-dimensional (0D) confinement [1] and single electron charging [2]. The zero-dimensional character can be utilized in new optoelectronic devices, such as low thresholds lasers [3], infrared detectors [3, 4] and high-density optical memories [5, 6].

In this review, I will describe the advantages of the Stranski–Krastanov technique for the growth of self-assembled QDs (Sect. 1). In Sects. 3 and 4, I will discuss the influence of high index planes and thin GaAs capping layers on the shape of InAs self-assembled

QDs, and the effects of growth interruption and $\text{Al}_y\text{Ga}_{1-y}\text{As}$ matrix layer on the luminescence emission of InAs/GaAs QDs. In Sect. 5, I will present resonant magnetotunnelling spectroscopy and show how this technique can produce full spatial maps of the wavefunction of the ground and excited states of electrons in a QD. In Sect. 6, I will report on progress of QD lasers. The paper concludes (Sect. 7) with a brief discussion of future applications of QDs.

Quantum dots fabrication

Several methods for the fabrication of QDs have been reported over the last decade including lithography-based technologies. Although this technique is widely used to provide QD predominantly by the combination of high-resolution electron beam lithography and etching, the spatial resolution required for reaching the size regime where significant quantization effects can be expected tends to be larger than the desirable level. In addition, lithographic methods and subsequent processings often produce contamination, defect formation, size non-uniformity, poor interface quality, and even damage to the bulk of the crystal itself. A new attractive method of defect free 10 nm scale QD fabrication is the Stranski–Krastanov (SK) growth in lattice-mismatched systems. In the SK growth mode the mismatched epitaxy is initially accommodated by biaxial compression in a layer-by-layer (2D) growth region, traditionally called the wetting layer. After deposition of a few monolayers the strain energy increases and the development of islands (3D) becomes more favourable than planar growth [7].

In the III–V semiconductor material system, SK growth has been used to grow InAs islands on GaAs and it has been shown that the size fluctuation of dots is relatively small ($\leq 10\%$) and the small dots and surrounding host matrix are dislocation-free and strained coherently with GaAs. It has been reported that the InAs growth mode changes from 2D to 3D upon the deposition of less than 2 monolayers of InAs, so as to reduce the strain in grown layer, since there is about a 7% lattice mismatch in the GaAs/InAs system. The strained (In,Ga)As/GaAs material system has been the most widely studied for which various quantum effects have been demonstrated. Various combinations of III–V semiconductors based on phosphorus or antimony compounds, and Si/SiGe alloys have also been studied.

The advantages of this technique of QD fabrication are that no nanotechnology and no further etch or implantation induced process is necessary. Since the dots are grown in-situ a homogeneous surface

morphology is maintained and defect creation is avoided. However, the inherent problem associated with this method is the size non-uniformity and the position uncontrollability of the QD. Controlling the dimension and arrangement of the self-organized 3D structures is thought to be very important for obtaining good properties of the structures.

The islands become technologically more interesting if it is possible to manipulate their arrangement laterally and vertically (Fig. 2) in order to achieve the 3D arrays. There are already several reports on spontaneous lateral ordering due to the preferential nucleation along surface steps. Kitamura et al. [8] demonstrated successful alignment of InGaAs by using a 2° off (100) GaAs substrate with multi-atomic steps in MOCVD growth process. Pre-patterned substrates have also been used for ordering of QDs in a more direct way. Miu et al. [9] grew by MBE on etched GaAs gratings and found islands to form on the side-walls of ridges running along [1–10] direction. Similar results were obtained by Jeppesen et al. [10] for Chemical Beam Epitaxy (CBE) deposited InAs islands in wet-etched and partially overgrown trenches and holes on a (100) GaAs surface. They formed chains of InAs islands aligned in trenches along [011]. The chains of islands have 33 nm minimum periods.

The vertical alignment is expected and the total density can be increased by stacking the QDs with a

spacer layer. Vertically aligned and electronically coupled islands has several advantages including the application of the tunnelling process to novel electronic devices such as single electron tunnelling devices, the study of tunnelling dynamics between QDs, and the high QD density for QD lasers. Several groups have recently successfully grown stacked InAs self-assembled QD structures separated by GaAs spacer layers by molecular beam epitaxy (MBE). Sugiyama et al. [11] reported vertically aligned InAs QDs up the ninth layer with 2.5 nm monolayers InAs and 1.5 nm GaAs spacer layers. Solomon et al. [12] demonstrated arrays of InAs islands which are vertically stacked, vertically aligned and electronically coupled in the growth direction. They have achieved vertical alignment of up to 10 islanding layers with no associated dislocation generation.

Controlling the shape of InAs self-assembled quantum dots

Influence of high index planes

To date, most studies of III–V semiconductor structures have concentrated on the conventional (100)-oriented substrates because of (i) the wide range of growth conditions which result in good epitaxial layer quality, (ii) the well-developed processing technology for this orientation, and (iii) the natural cleavage planes normal to the (100) orientation which are important in fabricating semiconductor devices, such as lasers. However, modulated semiconductor structures are likely to exhibit interesting phenomena which are strongly orientation-dependent because (i) interband transitions involve both the valence band (which depends strongly on crystallographic orientation) and the conduction band (which is hardly affected by it), (ii) growth kinetics depend on the surface orientation (Miller index), (iii) strain depends on the surface index when heterostructures are grown, and (iv) charge or surface polarity depend on the surface index. A new step forward in semiconductor material engineering involves the growth of epitaxial layers on high index planes, HIPs (i.e. other than (100)).

Key design parameters for QDs include size, shape, density, and spatial arrangement. After choosing the material system that allows QD formation, design flexibility is limited by the growth physics, usually determined by the temperature and growth rate of the epilayer. An alternative approach to influence the growth mode is to use high Miller index surfaces [13–18]. These provide different chemical potentials

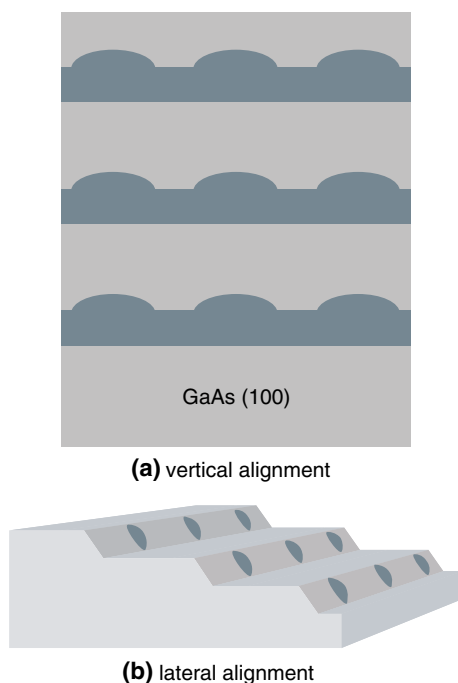


Fig. 2 Schematic diagram showing ordering of quantum dots due to strain fields effects to form (a) vertical alignment, and (b) lateral alignment on patterned substrates

for the deposited species and thus affect the kinetics of adsorption, migration, and desorption. Besides, the particular substrate orientation and reconstruction determines the strain relaxation mechanism. These effects have a large impact on the range of achievable island shapes, sizes, and ordering [19, 20]. The electronic levels are, in turn, determined by the QD shape and size: the correlation between design parameters, electronic structure, and optical properties is one of the main focuses of research in QD physics.

We have obtained self-assembled InAs QDs of highly non-conventional shape by using a GaAs(311)A and (311)B substrate (see Fig. 3). The QDs grown on (100) surfaces have a round dome shape, while the (311)A and (311)B dots display an arrow-head-like faceted [19] and pyramid shape, respectively. The arrow orientation is ordered and points along the $[-233]$ direction, which is related to a corrugation of (311)A surfaces.

Influence of thin GaAs capping layers

The morphology of QDs is strongly controlled by the growth conditions. Various QD shapes have been reported for InAs/GaAs self-assembled QDs including lenses [21, 22], square-base pyramids [23], truncated-pyramids [24] and elongated-pyramids [25]. The morphology and composition of the dot determines the electronic confinement potential and hence the QD

electronic energy spectrum and corresponding wavefunctions. It has been found that the surface morphology of the InAs QDs is strongly affected by the deposition a thin GaAs capping layer [26]. Ring-shaped QD structures were reported for InAs/GaAs QDs thermally annealed and capped with a thin GaAs layer [26]. However, the growth dynamics of such structures are not yet clear, in particular, with respect to small variations in the thickness of the capping layer or to the substrate orientation.

The InAs QD substrates were grown by molecular beam epitaxy (MBE) on (100)-oriented samples. Three series of samples were examined. In series S, an InAs layer of average thickness $L = 1.8, 2.0$ and 2.3 monolayers (MLs) was deposited on a $0.5\ \mu\text{m}$ GaAs buffer layer, at a growth temperature of $500\ ^\circ\text{C}$. Series A is identical to series S except for a $90\ \text{s}$ thermal annealing of the InAs layer at $530\ ^\circ\text{C}$. Finally, for series C layers, thin GaAs layers of various thicknesses were deposited on top of the InAs layer at $530\ ^\circ\text{C}$.

For all samples the growth rate for InAs and GaAs were 0.067 and $1\ \text{ML/s}$, respectively, and the As/Ga beam flux equivalent pressure as measured by an ion gauge was $12:1$.

Figure 4 shows AFM images ($1\ \mu\text{m} \times 1\ \mu\text{m}$) of samples of series S and A with an InAs coverage, L , equal to $1.8, 2.0$ and $2.3\ \text{MLs}$. The horizontal and vertical directions of the images correspond to the $\{0\ 1\ 1\}$ crystallographic directions. In samples of series S we observe dots with diameter $d \sim 30\ \text{nm}$ and height $h \sim 5\ \text{nm}$. The dot density increases with L from a value $\rho \sim 1.5 \times 10^{11}/\text{cm}^2$ for $L = 1.8\ \text{MLs}$ to $\rho \sim 2.0 \times 10^{11}/\text{cm}^2$ for $L = 2.3\ \text{MLs}$. The annealing affects both size and density of the dots. For samples A1 and A2 (panels d and e), corresponding to $L = 1.8$ and $2.0\ \text{MLs}$, respectively, the typical dot diameter is $d \sim 50\ \text{nm}$ and the typical height is $h \sim 7\ \text{nm}$. For sample A3 ($L = 2.3\ \text{MLs}$), the AFM image shows that the dot size distribution is unusual, comprising two types of dots with quite different sizes. The group of dots of smaller size have the same size as the dots in samples A1 and A2, but lower density $\rho \sim 1 \times 10^{10}\ \text{cm}^{-2}$. The other group of dots are bigger ($d \sim 80\ \text{nm}$, $h \sim 12\ \text{nm}$) with density $\rho \sim 2 \times 10^9\ \text{cm}^{-2}$. The analysis of the AFM images of the different samples shows that the annealing does not affect significantly the standard deviation, σ_d , of the dot diameter distribution ($\sigma_d \sim 0.25$).

The morphology of the InAs QDs changes significantly when, after the thermal annealing, they are capped by a thin layer of GaAs. Figure 5 shows AFM images ($1\ \mu\text{m} \times 1\ \mu\text{m}$) of a sample with $L = 2.3\ \text{InAs MLs}$ and GaAs capping layer equal to $1\ \text{nm}$ (sample

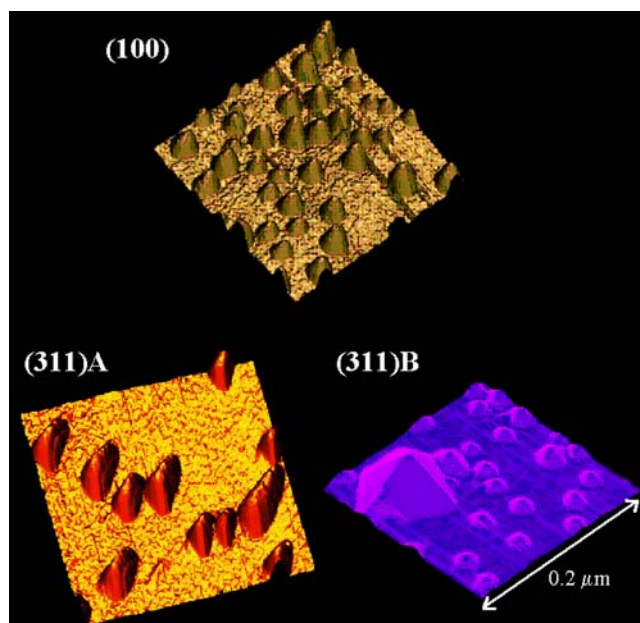
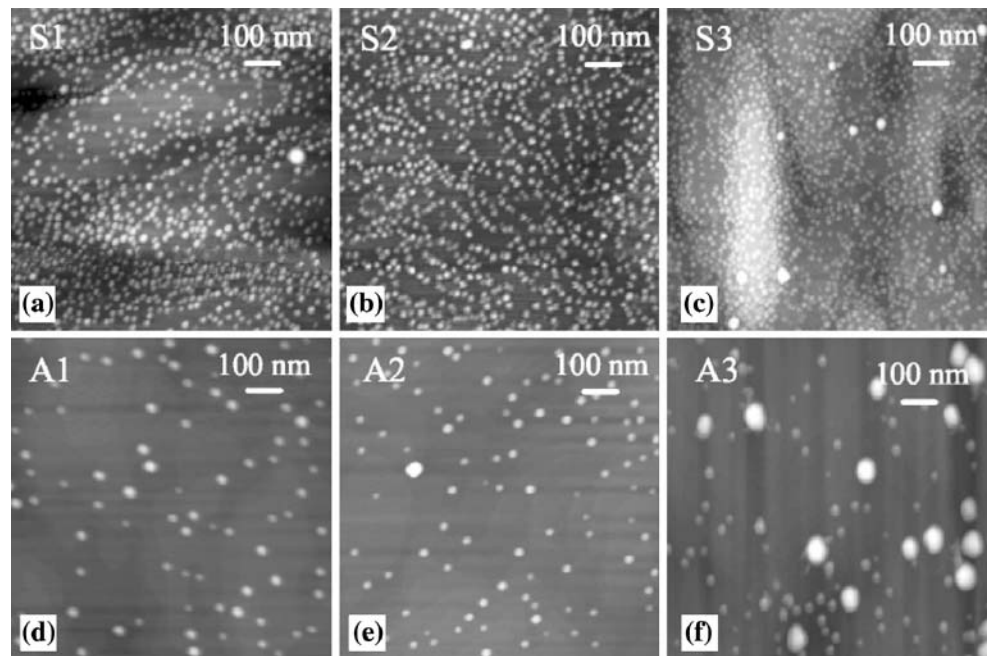


Fig. 3 Scanning tunnelling microscope pictures ($200 \times 200\ \text{nm}$) of InAs/GaAs QDs grown by MBE on (100), (311)A and (311)B GaAs substrates [7]. As can be seen, using substrates with different orientation can control the shape of the QDs [19]

Fig. 4 AFM pictures ($1 \times 1 \mu\text{m}$) of uncovered InAs QDs formed on a(100)-oriented GaAs substrate for an InAs coverage, L , equal to 1.8, 2.0 and 2.3 MLs without (a, b and c) and with annealing (d, e and f) [27]



C1, panel a), 2 nm (sample C2, panel b), 4 nm (sample C3, panel c) and 5.3 nm (sample C4, panel d). For all samples we observe a strong anisotropic shape. The dots are elongated along one of the $\{0\ 1\ 1\}$ directions in the (100) plane. Figure 5(e)–(h) show the vertical profile of the dot for scanning along one of the $\{0\ 1\ 1\}$ directions. Sample C1 shows “humped-back” dots with density and size comparable to those of the corresponding uncapped sample (A3), but different height, which is slightly reduced in sample C1. For sample C2, the central part of the humped-back structures is reduced in size, while the base is enlarged. For simplicity, we can consider the structure as a flat large dot with a “hump” on its top. For sample C3 the hump has evolved into a dip which increases in depth as we increase the cap layer thickness (sample C4). The dots are highly anisotropic and can be described as double

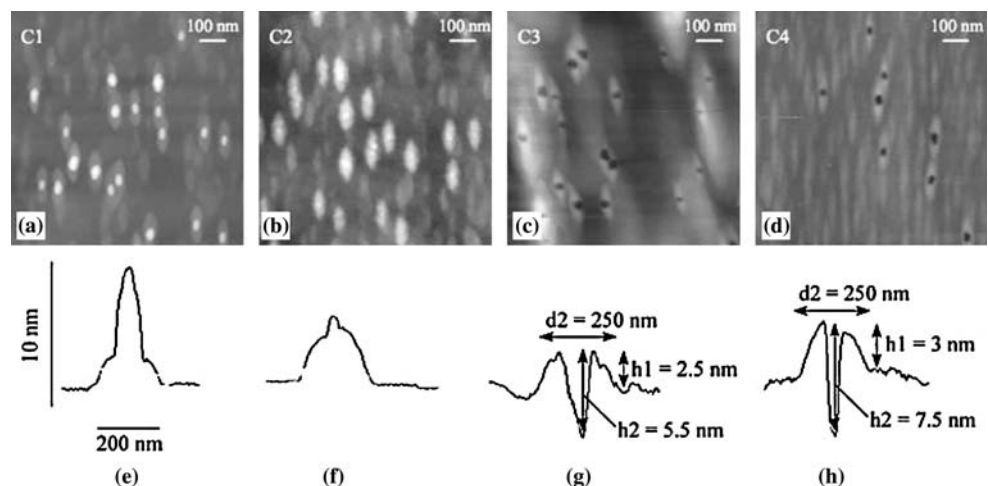
dot structures, or, using an alternative nomenclature, as anisotropic “rings”. Similar structures were observed in Ref. [28]. The in-plane sizes of the QD rings are $d1 = 70 \text{ nm}$ and $d2 = 250 \text{ nm}$. The typical height is $h1 = 2.5 \text{ nm}$ and the typical depth of the dip is $h2 = 5.5 \text{ nm}$ (see Fig. 5g). These morphological changes are explained in terms of indium diffusion from the dots into the cap layer [27].

Luminescence emission tuning of InAs/GaAs quantum dots

Effects of growth interruption

Here the effects of growth interruption on the optical and microscopic properties of InAs/GaAs

Fig. 5 AFM images ($1 \times 1 \mu\text{m}$) for a QD sample with an InAs coverage of 2.3 MLs after annealing and capping with a thin GaAs layer of thickness 1 nm (a), 2 nm (b), 4 nm (c) and 5.3 nm (d). Figure (e), (f), (g) and (h) show vertical profile of the dot for each sample [27]



self-assembled dots grown by MBE on (100) and (311)B oriented GaAs substrates are described. The growth interruption applied after the deposition of the InAs layer allows the formation of well-developed InAs dots (large dot size). This effect is enhanced in (311)B samples, where the growth interruption can be used to tune, in a controlled way, the emission energy and the luminescence intensity of the dots [29].

Samples were grown by MBE on a (100) and a (311)B oriented GaAs substrate, which were mounted side by side on the same substrate holder for comparison purposes. A 0.5 μm -thick GaAs buffer layer was grown, the first 0.2 μm at 580 $^{\circ}\text{C}$ and the remaining 0.3 μm at 600 $^{\circ}\text{C}$. Then the substrate temperature was reduced from 600 $^{\circ}\text{C}$ to a temperature 480 $^{\circ}\text{C}$ and a 1.8 monolayer (ML) thick InAs layer was deposited at a growth rate of 0.06 ML s^{-1} . Before completing the sample with a 25 nm-thick GaAs cap layer, the growth was interrupted under an As molecular flux. The As beam equivalent pressure as measured with an ionization gauge was 1.2×10^{-5} Torr. Different growth interruption times, τ_I , (0, 40, 80 and 120 s) were used.

Figure 6 shows the room temperature PL spectra of a series of (311)B samples having different growth interruption times. The main PL band, which is due to carrier recombination from the dots, shows a red shift with increasing τ_I . This effect is weaker at the highest τ_I , when a saturation of the red shift and a decrease of the QD PL intensity is observed. Similar effects are observed in the (100) samples, but less strongly. The dependence of the QD PL peak energy on τ_I at room temperature is shown in Fig. 7, for both the (311)B and the (100) samples.

It is believed that the growth interruption applied after the deposition of the strained layer could favour

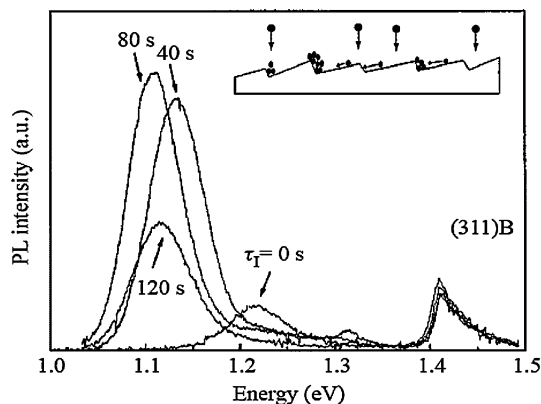


Fig. 6 Room temperature PL spectra of InAs/GaAs QDs grown on a (311)B oriented GaAs substrate. Samples are grown at 480 $^{\circ}\text{C}$ with a growth interruption time, τ_I , ranging between 0 and 120 s, by steps of 40 s. The inset shows a scheme for the dot nucleation on surface steps [29]

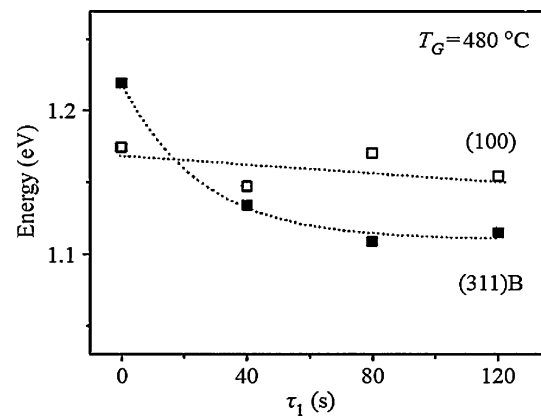


Fig. 7 Dependence of the QD PL peak energy on the growth interruption time, τ_I , for InAs/GaAs QDs grown on (311)B and (100) GaAs substrates at room temperature [29]

the surface atom transfer toward preferential sites on the growth plane, such as surface edge steps. The dots nucleate preferentially on these sites and they have time to increase their size in order to reach an equilibrium size and/or shape. Therefore, increasing τ_I favours the formation of well-developed dots and thus a red shift of the QD PL band. When the dot size becomes large, different processes occur such as the coalescence of the dots and/or their plastic relaxation. These latter mechanisms could account for the decrease of the dot PL efficiency at the highest τ_I (see Fig. 6).

The optical data are consistent with the TEM results. Figure 8a and b show, respectively, the cross-section TEM of two (311)B samples with growth interruption times of 0 and 120 s. The island morphology is revealed by the chemical compositional contrast between the InAs (dark regions) and the GaAs (bright regions) layer. For the sample with $\tau_I = 0$ s, the TEM image shows an inhomogeneous InAs layer made of small InAs islands. Increasing the growth interruption time causes a drastic increase in the size of the islands, which become well-developed dots with a pyramidal shape. As shown by the arrows in Fig. 8b, the largest dots produce deep holes in the GaAs cap layer.

The influence of the growth interruption on the dot optical and microscopic properties shows that the dot nucleation is affected by kinetic mechanisms and that they are stronger in the (311)B samples. The difference between the (100) and the (311)B samples can be explained in terms of a different configuration for the GaAs surface: different preferential sites for the dot nucleation could be present on the growth plane. This hypothesis is consistent with recent atomic force microscopy (AFM) measurements reported in Ref.

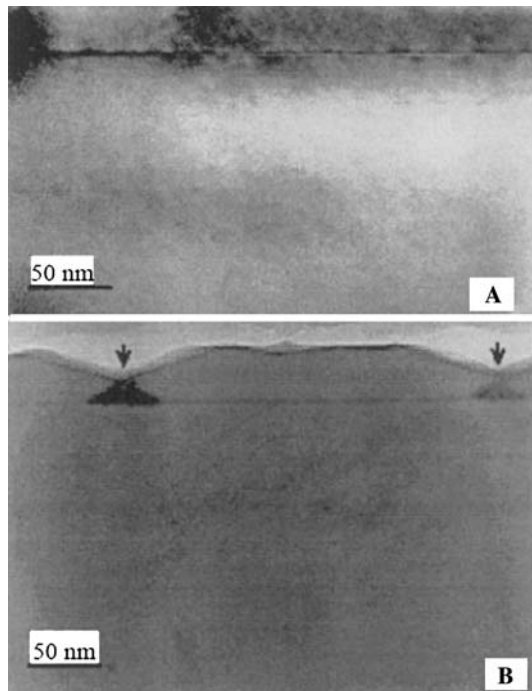


Fig. 8 Cross-section TEM of InAs/GaAs QDs grown on a (311)B oriented GaAs substrate, with a growth interruption time, τ_I , equal to 0 and 120 s and a growth temperature equal to 480 °C [29]

[30], which show a (311)B oriented GaAs surface made of grooves. These structures, which are absent on the (100) substrates, could affect the dot formation.

Effects of $\text{Al}_y\text{Ga}_{1-y}\text{As}$ matrix layer

In this section the photoluminescence properties of multiple (InGa)As/(AlGa)As QD layers grown by MBE under different conditions (i.e., different Al content, number of QD layers, and different spacer thickness between QD layers) are reported. We found that by varying the Al content in the (AlGa)As matrix and/or stacking several QD layers, the room temperature dot luminescence is tuned over a wavelength range from 0.8 μm to 1.3 μm [31].

Three different sets of samples were considered. In the first set, three InAs layers were embedded in an $\text{Al}_y\text{Ga}_{1-y}\text{As}$ matrix grown at $T_G = 520$ °C. The average thickness, L , of each InAs layer is 1.8 monolayer, ML. The three InAs layers are separated from each other by 20 nm-thick $\text{Al}_y\text{Ga}_{1-y}\text{As}$ barriers ($y = (0.0-0.8)$), resulting in uncoupled dots. In the second set, 1 and 10 layers of InAs dots ($L = 1.8$ ML) were embedded in a GaAs matrix. The vertically stacked InAs layers were separated from each other by a distance $d = 1.7$ nm. This structure was grown at $T_G = 500$ °C. Finally, in the third set of samples, three

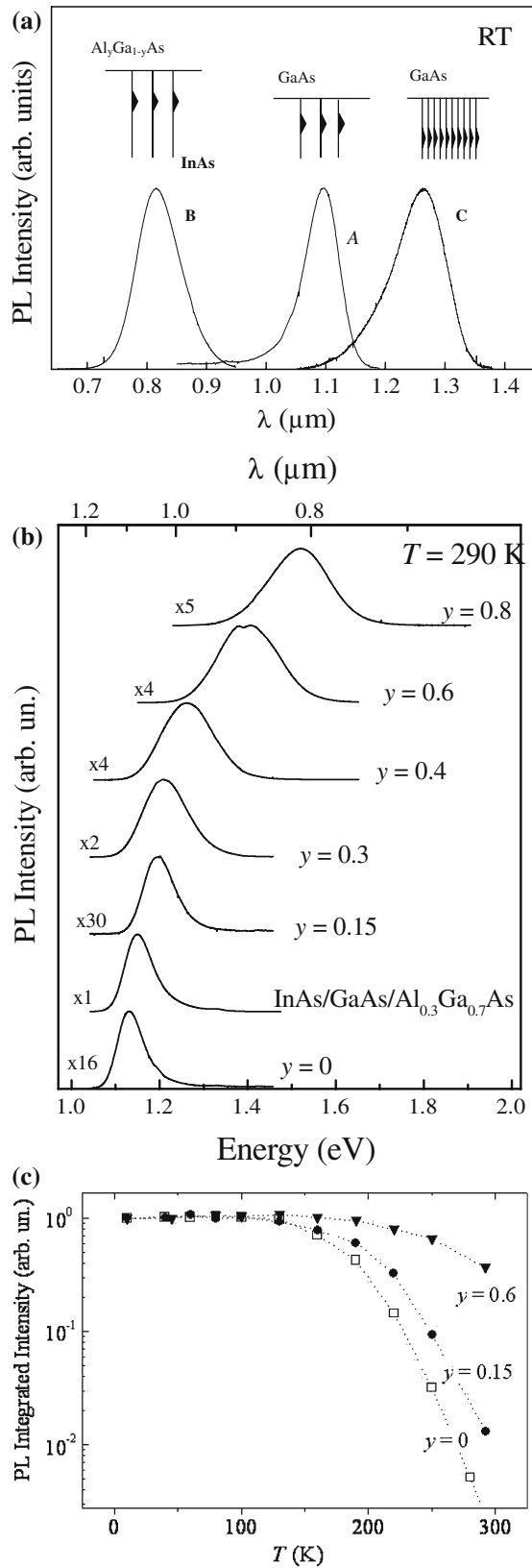
InAs layers were embedded each of them in a GaAs/ $\text{Al}_{0.3}\text{Ga}_{0.7}\text{As}$ quantum well and grown at $T_G = 500$ °C. The dot formation was controlled in situ by monitoring the reflection high-energy electron-diffraction pattern. Photoluminescence measurements were performed from $T = 10$ K to $T \sim 500$ K. The optical excitation was provided by the 514.5 nm line of an Ar^+ laser. The luminescence was dispersed by a 3/4 m monochromator and detected by a cooled Ge diode.

Figure 9(a) shows the room temperature QD PL emission for three representatives InAs QD samples. The three samples have different Al content in the $\text{Al}_y\text{Ga}_{1-y}\text{As}$ matrix surrounding the dots or have different spacing (d) or number (N) of the InAs QD layers. With increasing y , the QD PL band blue-shifts from 1.1 μm (sample A: $y = 0$, $d = 20$ nm, $N = 3$) to 0.8 μm (sample B: $y = 0.8$, $d = 20$ nm, $N = 3$) (see also Fig. 9(b)). This blue-shift is due to the deeper carrier confining potential of the dots at higher values of y . In contrast, with decreasing d and/or increasing N , the PL red-shifts from 1.1 μm (sample A: $y = 0$, $d = 20$ nm, $N = 3$) to ~ 1.3 μm , (sample C: $y = 0$, $d = 1.7$ nm, $N = 10$), evidence for electronic coupling between vertically stacked QDs. Therefore by engineering the carrier potential profile of the dots it is possible to cover a broad energy range for the room temperature light emission of QDs [32]. This is of particular interest for extending the optical emission range of QDs to 1.3 μm , the window for signal transmission through silica fibers.

Room temperature PL emissions of the set of samples which consist of three InAs layers separated from each other by 20 nm-thick $\text{Al}_y\text{Ga}_{1-y}\text{As}$ barriers ($y = (0.0-0.8)$) are shown in Fig. 9(b). These samples exhibit a different thermal behaviour (see Fig. 9(c)). In fact the thermal stability of the dot emission is strongly dependent on the composition of the matrix incorporating the dots. We found that the dots embedded in a (AlGa)As barrier and/or in a GaAs/(AlGa)As QW exhibit the highest thermal stability [32]. This can be attributed to the low level of thermal escape of carriers from the dots towards the high energy levels of the AlGaAs barrier or the GaAs/(AlGa)As QW, which therefore act to prevent carrier depopulation of the dot levels.

Magneto-tunnelling spectroscopy for spatial mapping of wavefunctions of the electronic states in self-assembled quantum dots

In this section, the technique of resonant magneto-tunnelling spectroscopy (RMTS) is used to show how



this non-invasive and non-destructive technique can produce full spatial maps of the wavefunction of the ground and excited states of electrons in a QD.

Fig. 9 (a) Room temperature PL spectra of samples A (InAs/GaAs QDs, $d = 20$ nm), B (InAs/ $\text{Al}_{0.8}\text{Ga}_{0.2}\text{As}$ QDs, $d = 20$ nm) and C (vertically stacked InAs/GaAs QDs, $d = 1.7$ nm and $N = 10$) [31]. The inset sketches the structure for the three samples. (b) Room-temperature PL spectra of InAs/ $\text{Al}_y\text{Ga}_{1-y}\text{As}$ self-assembled quantum dots for different Al content y [32]. (c) Temperature dependence of the PL integrated intensity for InAs/GaAs open squares, InAs/ $\text{Al}_{0.15}\text{Ga}_{0.85}\text{As}$ closed circles, and InAs/ $\text{Al}_{0.6}\text{Ga}_{0.4}\text{As}$ closed triangles quantum dots [32]. The lines are guides for the eye

In a RMTS experiment, the application of a magnetic field, B , perpendicular to the tunnel current introduces a change Δk_{\parallel} in the momentum component of the tunnelling electron parallel to the tunnel barriers and perpendicular to B [33]

$$\hbar \Delta k_{\parallel} = eB\Delta s \quad (1)$$

where Δs is the effective tunnelling distance. The formula can be understood in terms of the action of the Lorentz force on the tunnelling electron. An early application of this effect was to use the magnetic field to vary the k -vector of carriers tunnelling from extended emitter states into extended states in the QW. The applied voltage provides a means of tuning into the energy of a particular state in the QW; the applied field shifts the k -vector. The method proved an effective probe of the energy dispersion curves of quasi-1D skipping states [33] and bound states in QWs [34].

In RMTS, the tunnel current is proportional to the modulus squared of the matrix element between the initial and final states of the tunnel transition. The B dependence of the current can be expressed by the modulus squared of the overlap integral [35, 36], represented in k -space as

$$I \sim \left| \int_{-\infty}^{+\infty} \varphi_e(k - \Delta k_{\parallel}) \varphi_c(k) dk \right|^2 \quad (2)$$

where $\varphi_e(k)$ and $\varphi_c(k)$ are the Fourier transforms of the real space wavefunction of the emitter state and the final state, respectively.

Equations (1) and (2) imply that B can provide a means of measuring $\varphi_c(k)$ with a resolution in k -space given by the width of $\varphi_e(k)$. In particular, since the initial state in the emitter has only weak spatial confinement, $\varphi_e(k)$ corresponds to a sharply peaked function with a finite value only close to $k = 0$. Therefore, the intensity of the resonant current feature associated with the confined state is given approximately by $|\varphi_c(k)|^2$.

The RMTS method may be regarded as complementary to scanning tunnelling microscopy (STM) and

related techniques [37], which are powerful tools for imaging electronic states on or close to condensed matter surfaces. In that case, the moving tip acts as a probe of the wavefunction in real space. In RMTS, the magnetic field acts as a variable probe in k -space. An advantage of RMTS is that it can be used to probe states that are well away from the surface of a sample.

The structures used in this work were grown on (100) and (311)B substrates by MBE in a Varian Gen-II machine under the same conditions so as to render them comparable. The layer composition of our devices is shown schematically in Fig. 10.

A layer of InAs self-assembled QDs is embedded in the center of an undoped 12-nm GaAs quantum well (QW), which is sandwiched between two 8.3-nm $\text{Al}_{0.4}\text{Ga}_{0.6}\text{As}$ tunnel barriers. The layer of InAs QDs was grown by depositing 2.3 monolayers (ML) of InAs. Undoped GaAs spacer layers of width 50 nm separate the barriers from two contact layers with graded n-type doping [38]. The device acts as a resonant tunnelling diode in which electrons can tunnel into the QD from a doped contact layer on the opposite side of the barrier. Mesas were fabricated from each wafer by photolithography and wet chemical etching techniques. Au/Ge/Ni ohmic contacts were formed by evaporation and alloying. The bottom contact was made to the back of the substrate. Here we focus on a structure grown on a (311)B-oriented GaAs substrate, although we have obtained similar results for dots grown on (100)-oriented GaAs. For comparison, we also studied a control sample grown with the same sequence of layers, but with no InAs layer.

Figure 11 shows the current–voltage characteristics, $I(V)$, for samples with QDs (sample qd) and without QDs (sample c) in negative bias (positive substrate).

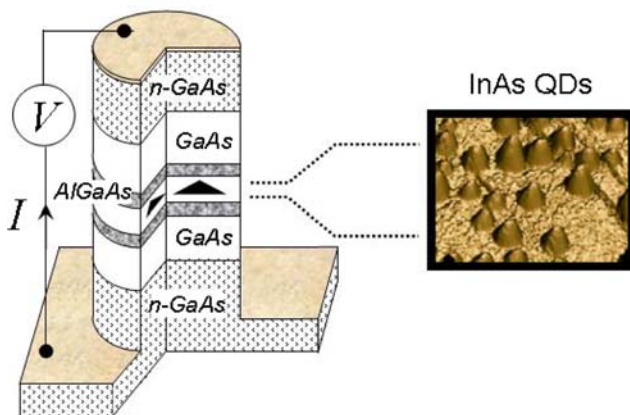


Fig. 10 Schematic diagram of a n-i-n GaAs/(AlGa)As RTD incorporating a layer of quantum dots (QDs) in the centre of the GaAs well

At low bias, they differ substantially: in the control sample we observe a single resonance due to electrons tunnelling through the first quasi-bound state of the QW; in contrast, in sample qd, the current is strongly suppressed and a multitude of low-current resonant peaks can be observed.

The resonant current features observed in sample qd are related to the presence of the InAs QDs. In particular, for each feature, we observe a thermally-activated current onset, which is an unambiguous signature of an electron tunnelling from a thermalized Fermi-distribution of emitter states into an individual, discrete QD energy level [40].

Note that the potential profile of the RTD with the dots is different from that of a RTD without dots. In the former case, the layer of InAs QDs introduces a set of discrete electronic states below the GaAs conduction band edge. At zero bias, equilibrium is established by some electrons diffusing from the doped GaAs layers and filling the dot states. The resulting negative charge in the QW produces depletion layers in the region beyond the (AlGa)As barriers thus producing an effective tunnel barrier that is wider and higher than in the case of the control sample (see the inset of Fig. 10). When a voltage, V , is applied, resonant tunnelling through a particular QD state leads to a peak in the current–voltage plot, $I(V)$, whenever the energy of the state is resonant with an adjacent filled state in the negatively biased electron emitter layer, located at the left of the tunnel barriers.

In the following, the magnetic field dependence of the electron tunnelling through the QD states will be

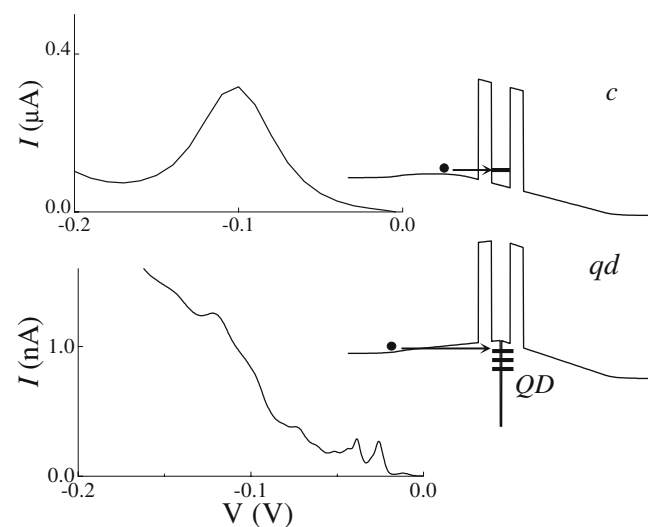


Fig. 11 $I(V)$ characteristics at 4.2 K for samples qd and c. Inset: Sketch of the conduction band profile of the two samples under an applied bias [39]

presented and it will be shown how resonant magnetotunnelling can map out the probability density of the quantum-confined states in self-assembled QDs.

Figure 12 shows the low-temperature ($T = 4.2$ K) $I(V)$ characteristics in reverse bias (positive biased substrate) in the presence of a magnetic field, B , applied parallel to the growth plane (X , Y). A series of resonant features labelled e_1 – e_7 are observed. The resonant peaks are not observed in samples with no dots, so they are related directly to the presence of InAs QD layer.

The amplitude of each resonance exhibits a strong dependence on the intensity of B . In particular, we can identify three characteristics types of magnetic field dependence: type I (peaks e_1 , e_2 , e_3) shows a maximum in I at $B = 0$ T followed by an almost monotonic decay to zero at around 8 T; type II (e_4 and e_5) shows a broad maximum in I at ~ 4 T, followed by a gradual decay to zero; type III (e_6 and e_7) shows two clear maxima in I at $B = 0$ T and ~ 5 T, with I falling to a minimum value of almost zero between these maxima.

The magnetic field dependence of the resonances can be understood in terms of the effect of B on a tunnelling electron. The applied voltage allows tuning resonantly to the energy of a particular QD state.

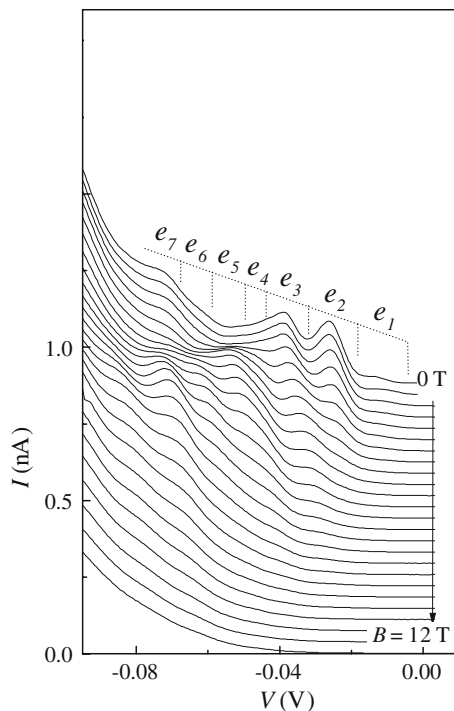


Fig. 12 Low-temperature ($T = 4.2$ K) $I(V)$ characteristics in reverse bias (positive biased substrate) in the presence of a magnetic field, B , perpendicular to the current. B is increased in steps of 0.5 T and the corresponding curves are displaced along the current axis for clarity [39]

Then, by measuring the variation of the tunnel current with B , one can determine the size of the matrix element that governs the quantum transition of an electron as it tunnels from a state in the emitter layer into a QD.

Equations (2) and (3) imply that the magnetic field can provide a means of measuring $\varphi_{\text{QD}}(k)$ the wavefunction of a QD state. As before, the intensity of the resonant current feature associated with the QD state is given approximately by $|\varphi_{\text{QD}}(k)|^2$. Thus by plotting $I(B)$ for a particular direction of B we can measure the dependence of $|\varphi_{\text{QD}}(k)|^2$ along the k -direction perpendicular to B . Then, by rotating B in the plane (X , Y) and making a series of measurements of $I(B)$ with B set at regular intervals of the rotation angle, we obtain a full spatial profile of $|\varphi_{\text{QD}}(k)|^2$. This represents the projection in k -space of the probability density of a given electronic state confined in the QD [39].

Figure 13 shows the form of the differential conductance $G(B) = dI/dV(B) \sim |\varphi_{\text{QD}}(k)|^2$, in the plane (k_x , k_y) for three representative QD states. The contour plots reveal clearly the characteristic form of the probability density distribution of a ground state orbital and the characteristic lobes of the higher energy states of the QD. The electron wavefunction has a biaxial symmetry in the growth plane, with axes corresponding quite closely to the main crystallographic directions $[01\bar{1}]$ and $[\bar{1}23]$. For a similar InAs QD structure grown on a (100) substrate we also obtained characteristic probability density maps of ground and excited states.

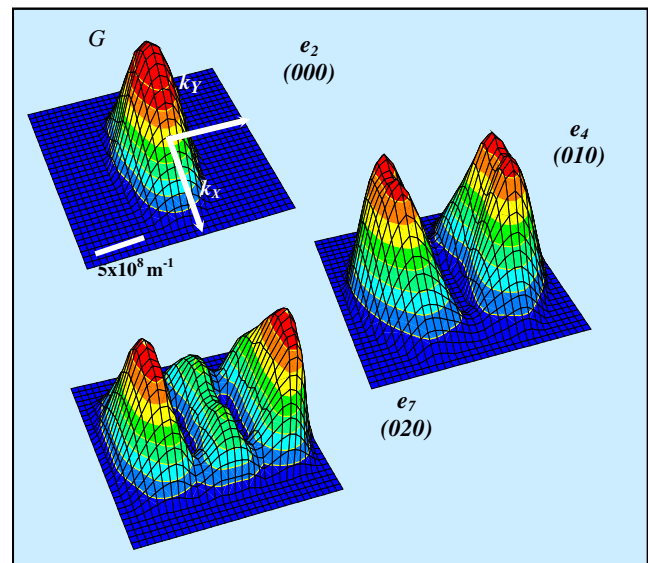


Fig. 13 Distribution in the plane (k_x , k_y) of the conductance, $G(B)$, for three representative states associated to the resonances e_2 , e_4 , and e_7 shown in the Fig. 12

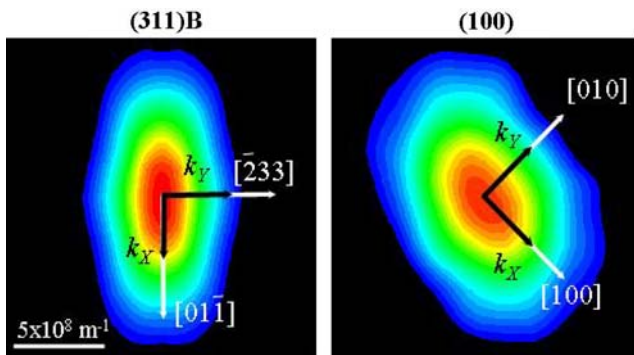


Fig. 14 Plot shows the distribution of $I(B) \sim |\varphi_{\text{QD}}(k_x, k_y)|^2$ in the plane (k_x, k_y) at $T=4.2$ K [41]. Red colour corresponds to higher normalized current values. The main crystallographic axes for each substrate orientation are indicated

Figure 14 shows plots of the probability densities associated with the QD ground states for resonant tunnelling diodes with substrate orientations (311)B and (100). In both cases, the projected probability density has elliptical form in the plane (k_x, k_y) . For the (100) case, the axis of electron wavefunction symmetry is at an angle $\sim 30^\circ$ relative to the main crystallographic direction $[1-10]$, i.e. it is inclined at around 15° to $[100]$. These data suggests that the QDs have elongated shapes for both substrate orientations.

Several different methods have been used to calculate the eigenstates of QDs, including perturbation effective mass approaches [42], 8-band k.p theory [43] and empirical pseudopotential models [44]. The wavefunctions are usually presented as plots of the probability density in real space, $|\varphi_{\text{QD}}(r)|^2$. A tunnel current measurement can provide no information about the phase of the wavefunction but, in general, the phase of $\varphi_{\text{QD}}(r)$ emerges naturally from the calculations. Once the phase factor is known, it is a straightforward task for theoreticians to Fourier transforms the wavefunction into k -space. A direct comparison could then be made with our $I(B)$ plots.

Quantum dot lasers

QDs find significant interest especially for application in laser diodes. It is worth noting that the device, which benefited most from the introduction of quantum wells (QW), is the injection laser. The QW laser reached mass production within very few years because of its low cost, high performance and high reliability. QDs are believed to provide a promising way for a new generation of optical light sources such as injection lasers. QD lasers are expected to have superior properties with respect to conventional QW lasers. Lower

threshold currents and higher characteristic temperature T_0 have been predicted for QD lasers (see Fig. 15).

The principal advantage of using size-quantized heterostructures in lasers originates from the increase of the density of states for charge carriers near the band-edges [Fig. 1(d)]. When used as an active medium of a laser, this results in the concentration of most of the injected non-equilibrium carriers in an increasingly narrow energy range near the bottom of the conduction band and/or top of the valence band. This enhances the maximum material gain and reduces the influence of temperature on the device performance. Figure 16 shows the development of semiconductor diode lasers in terms of threshold current density as a function of time for various heterostructures based on double heterostructure (DHS), QWs and QDs.

Lasing at room temperature with threshold current of 950 A/cm^2 from single layer of InGaAs QDs in an AlGaAs injection laser structure was demonstrated by Kirstaedter et al. [48]. A value of the characteristic temperature T_0 of 350 K in the temperature range 50–120 K and a threshold current of 120 A/cm^2 were found. This T_0 value is much higher than the theoretical prediction of 285 K for QW lasers.

Shoji and co-workers at Fujitsu Laboratories Ltd., Atsugi, Japan [49] achieved laser oscillation from self-organized $\text{In}_{0.5}\text{Ga}_{0.5}\text{As}$ QDs at 80 K by current injection. The dots were grown by Atomic Layer Epitaxy. The current density was 815 A/cm^2 and the lasing wavelength was 911 nm at 80 K. The observed laser oscillation is from a high order sublevel of QDs. The dots were 20 nm in diameter and 10 nm in height and

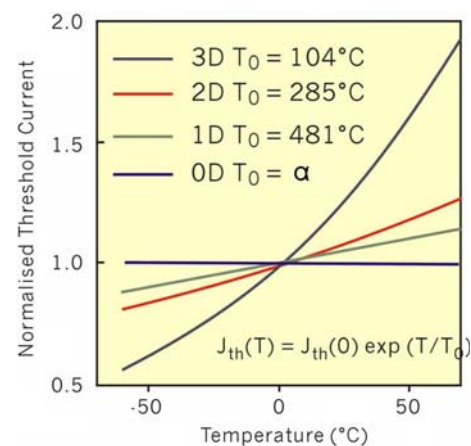
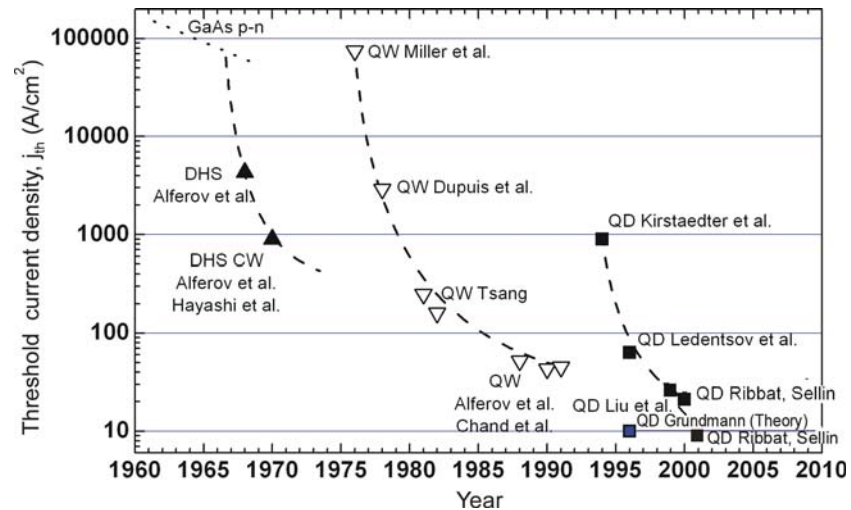


Fig. 15 Theoretical predictions of the threshold current versus temperature in double heterostructure (DHS), quantum well (QWs), quantum wire and quantum box (QDs) laser. The threshold current as a function of temperature T is given by: $J_{\text{th}}(T) = J_{\text{th}}(0) \cdot \exp(T/T_0)$ where T_0 is the laser characteristic

Fig. 16 Development of semiconductor diode lasers based on DHS, QWs and QDs [45]. The lowest current density achieved up to now is 6 A/cm² [46, 47]. Courtesy of D. Bimberg, Technical University of Berlin



were surrounded by InGaAs barriers in the lateral direction and by 100 nm thick GaAs separate confinement heterostructures (SCH) layers. It was believed that by increasing the uniformity of dot size, the aerial coverage, and the number of dot layers would lead to lasing at a lower sublevel, resulting in excellent performance at room temperature.

Laser operation of vertically coupled QDs was found to improve largely as compared to single QD lasers and room temperature operation, via the QD ground state, with a threshold current density of 680 A/cm² is obtained for a triple stack of QDs [50]. The same team reported the reduction of the threshold current density at 300 K down to 90 A/cm² and 60 A/cm² for 10 InGaAs QD stack in GaAs and AlGaAs matrix, respectively [51].

Xie et al. [52] reported the first observation of lasing in edge emitting graded index separate confinement heterostructures (GRIN-SCH) containing vertically self-assembled multiple stacks of electronically uncoupled InAs 3D islands in the active region grown by MBE. A low threshold current density of 310 A/cm² at 79 K is found for a stack of five sets of islands corresponding to two monolayers of InAs depositions separated by 36 monolayers of GaAs spacers grown by migration enhanced epitaxy (MEE). The distribution of the island volumes gave a multitude of laser lines between 980 nm and 996 nm.

The recent developed QD lasers [53] based on InAs QD system have already showed record low threshold current density of 24 A/cm² at room temperature for a wavelength of 1.28 μ m. This is almost a factor of two lower than what has been achieved for QW lasers [54]. InAs QD laser diodes with high light output power of 3 W at 1.1 μ m and 4.7 W at 1.135 μ m were also reported [55, 56].

It is possible to access new energies by combining materials with different lattice constants and energy gaps. Currently, the spectral range of III–V semiconductor QD lasers extends from near infrared 1.84 μ m for InAs–(In,Ga,Al)As QD lasers on InP substrates [57] to the visible red range [58].

Lasers based on InGaAsP/InP heterostructures emitting at 1.3 and 1.55 μ m are currently widely used in fiber optical communication systems. These lasers, which are mainly used for long-distance data transmission, are quite expensive. InAs/GaAs quantum dots are currently considered as the most promising candidates for this wavelength range. Park et al. [59] reported continuous-wave (CW) lasing of a single layer 1.3 μ m GaAs-based QD laser. The low CW current density of 45 A/cm² demonstrates the potential of this system for eventually realizing high performance lasers, and their potential application to optical interconnects.

Room temperature 1.3 μ m edge-emitting lasers using InGaAs QD structures grown by molecular beam epitaxy on GaAs substrates were demonstrated by several groups using various approaches. These include sub-monolayer deposition [60], low growth rate [61] and InGaAs overgrowth [62, 63]. Recently it was found [64] that multiple layers (up to 10) of InAs/InGaAs/GaAs quantum dots considerably enhance the optical gain of quantum dot lasers emitting around 1.3 μ m. A differential efficiency as high as 88% has been achieved in these lasers. Emission wavelengths of 1.28 μ m, threshold current density of 147 A/cm², differential efficiency of 80%, and characteristic temperature of 150 K have been realized simultaneously in one device (see Fig. 17).

There are only very few reports on the optimization of growth conditions for InGaAs/InP QDs emitting at

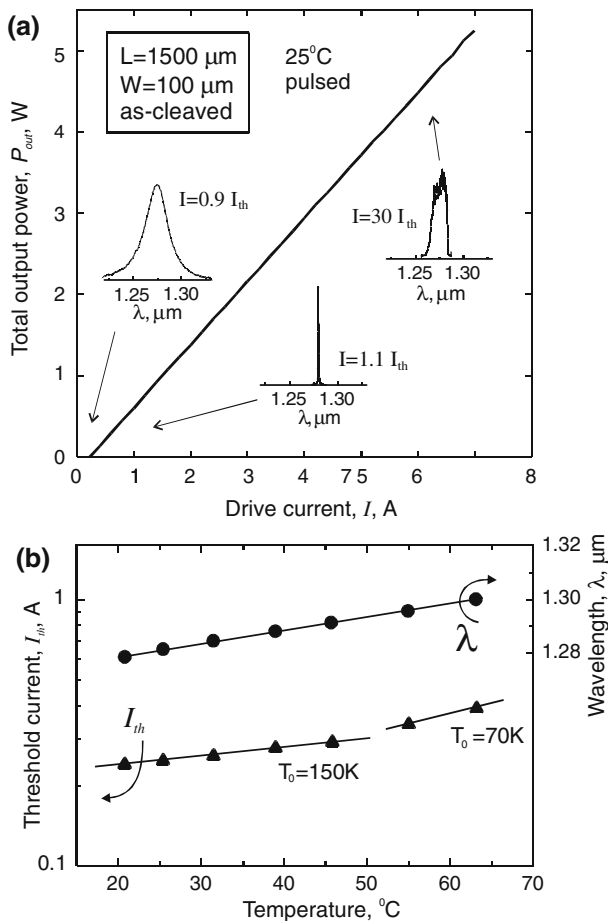


Fig. 17 Characteristics of 100 μm wide and 1.5 mm long diode based on 10 QD layers: (a) Dependence of the output power, P_{out} , from both facets on drive current, I , at room temperature and emission spectra recorded at different currents: (b) temperature dependences of lasing wavelength, λ , (solid circles) and threshold current, I_{th} , (solid triangles) [64]. Courtesy of N.N. Ledentsov, Ioffe Institute, St. Petersburg

1.55 μm , which is the most important wavelength in optical fiber telecommunications. Jang et al. [65] have optimized the growth conditions for the InGaAs/InGaAsP/InP QDs and demonstrated QDs of high luminescence efficiency and QD lasers operating at room temperature. InGaAsP with a bandgap energy lower than that of InP has been used for the QD barriers. An emission wavelength around 1.55 μm has been achieved and was controlled by the Ga composition in the InGaAs QDs.

Maksimov et al. [66] demonstrated lasing at a wavelength between 1.4 and 1.5 μm in QDs grown on GaAs substrates. The threshold current density and differential efficiency of lasers with a 1.5-mm-long cavity were, respectively, 2 kA/cm^2 and 50%. A high output power of 7 W at room temperature in pulsed mode was obtained. To reach this spectral range, the

structures were grown on a metamorphic $\text{In}_{0.2}\text{Ga}_{0.8}\text{As}$ buffer layer.

Very recently, high-power 1.3 μm InAs/GaInAs/GaAs QD lasers grown in a multiwafer Molecular beam Epitaxy (MBE) production system have been reported. The active region is based on multiple stacks of InAs/GaInAs/GaAs QD. Threshold current density of 190 A/cm^2 and high differential quantum efficiency of 70% were obtained at room temperature. These excellent values in addition to good I–V characteristics (1.1 V turn on voltage and series resistance as low as $2 \times 10^{-4} \Omega\text{cm}^2$) led to record continuous wave (CW) output power of 4.2 W for broad area devices (100 μm wide, 1600 μm long) [67].

The semiconductor lasers have opened up potentially huge markets in optical communication, compact disks and related optical data storage applications, displays and lighting. Until a very few years most of these lasers are edge emitters where the lasing cavity lies horizontally in the wafer plane. For many applications requiring for example a 2D laser array, it is desirable to have the laser output normal to the surface of the wafer. Such new breed of lasers is known as vertical-cavity surface-emitting lasers (VCSELs). Due to its unique topology, the VCSEL has some distinct advantages over the conventional edge-emitting laser. The optical beam is circular such that high coupling efficiency to optical fibres is available. The active volume of VCSELs can be made so small that high packing density, low threshold lasers are obtained. The design of the laser allows simple monolithic integration of 2D arrays of laser diodes, realizing interesting light sources for 2D optical data processing. Now there is a strong motivation to create long wavelength VCSEL using QD as the active medium. One of the advantages of using QDs in a VCSEL structure is that the non-equilibrium carriers are localized in the QDs and therefore the spreading of nonequilibrium carriers out of the injection region can be suppressed. This results in ultra-low threshold currents (Fig. 18) at ultra-small apertures [46, 47].

Conclusion

Semiconductor heterostructures containing self-assembled QDs are of fundamental interest because they provide a relatively simple means of producing an array of quantum potentials in which electrons and holes are confined in discrete quasi-atomic (or zero-dimensional) energy states. This offers considerable potential for applications in laser diodes and other novel optoelectronic devices, and for quantum-functional and memory

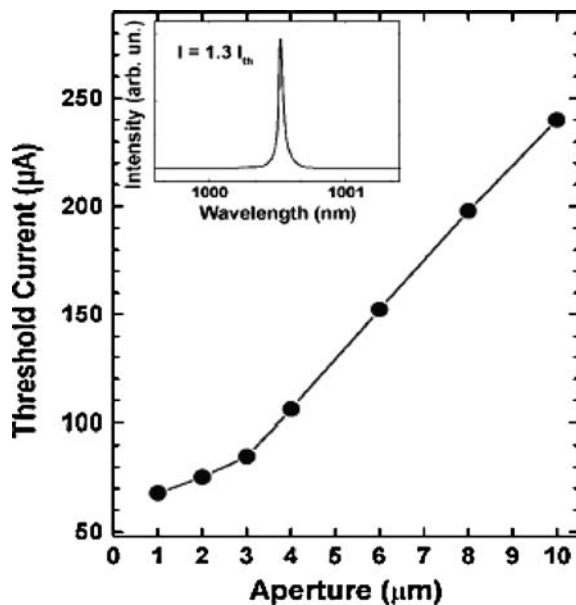


Fig. 18 QD VCSEL with ultrasmall apertures. CW low threshold current densities (170 A/cm^2 at 300 K, $10 \mu\text{m}$) and $70 \mu\text{A}$ threshold current ($1 \mu\text{m}$ oxide aperture) [46, 47]. Courtesy of N.N. Ledenstov, Ioffe Institute, St. Petersburg

devices. However, many challenges remain in the development of high-performance QD devices.

Acknowledgments This work is supported by the Engineering and Physical Sciences Research Council (U.K.) and the SANDiE Network of Excellence of the European Commission (Contract no. NMP4-CT-2004-500101). I am grateful to L. Eaves, A. Patane, A. Polimeni, P.C. Main, K. Takehana, F. Pulizzi, A. Levin, S. Sanguinetti, M. Guzzi, M.D. Upward, P. Moriarty, M. Al-Khafaji, A.G. Cullis, E.E. Vdovin, Yu.N. Khanin, Yu.V. Dubrovskii, G. Hill, D. Granados, J.M. Garcia, N.N. Ledenstov and D. Bimberg for their contribution to this work.

References

1. M.A. Reed et al., Phys. Rev. Lett. **60**, 535 (1988)
2. R.C. Ashoori et al., Phys. Rev. Lett. **68**, 3088 (1992)
3. D. Bimberg, M. Grundmann, N.N. Ledetsov, *Quantum Dot Heterostructures* (Wiley, Chichester, 1998)
4. L. Chu et al., Appl. Phys. Lett. **75**, 3599 (1999)
5. S. Muto, Jpn. J. Appl. Phys. **34**, 210 (1995)
6. Y. Sugiyama et al., Physica E **7**, 503 (2000)
7. M. Henini et al., Microelectron. J. **28**, 933 (1997)
8. N. Kitamura et al., Appl. Phys. Lett. **66**, 3663 (1995)
9. D.S.L. Miu et al., Appl. Phys. Lett. **66**, 1620 (1995)
10. S. Jeppesen et al., Appl. Phys. Lett. **68**, 2228 (1996)
11. Y. Sugiyama et al., Jpn. J. Appl. Phys. **35**, 1320 (1996)
12. G.S. Solomon et al., Phys. Rev. Lett. **76**, 952 (1996)
13. R. Notzel et al., Jpn. J. Appl. Phys. Part 2 **33**, L275 (1994)
14. R. Notzel et al., Nature (London) **369**, 131 (1994)
15. R. Notzel et al., Appl. Phys. Lett. **65**, 457 (1994)
16. K. Nishi et al., J. Appl. Phys. **80**, 3466 (1996)
17. D.I. Lubyshchev et al., J. Vac. Sci. Tech. B **14**, 2212 (1996)
18. C.M. Reaves et al., Appl. Phys. Lett. **69**, 3878 (1996)
19. M. Henini et al., Phys. Rev. B **57**, R6815 (1998)
20. K. Nishi et al., Appl. Phys. Lett. **70**, 3579 (1997)
21. J.M. Moison et al., Appl. Phys. Lett. **64**, 196 (1994)
22. J. Zou et al., Phys. Rev. B **59**, 12273 (1999)
23. S. Ruvimov et al., Phys. Rev. Lett. **84**, 334 (2000)
24. N. Liu et al., Phys. Rev. Lett. **84**, 334 (2000)
25. W. Yang et al., Phys. Rev. B **61**, 2784 (2000)
26. J.M. Garcia et al., Appl. Phys. Lett. **71**, 1014 (1997)
27. K. Takehana et al., J. Cryst. Growth **251**, 155 (2003)
28. I. Kamiya et al., J. Crystal Growth **201/202**, 1146 (1999)
29. A. Patane et al., Superlattices Microstruct. **25**(1/2), 113 (1999)
30. M. Kawabe et al., Jap. J. Appl. Phys. **36**, 4078 (1997)
31. M. Henini et al., Microelectron. J. **33**, 313 (2002)
32. A. Polimeni et al., Phys. Rev. B **59**, 5064 (1999); A. Patane et al., Appl. Phys. Lett. **75**, 814 (1999)
33. B.R. Snell et al., Phys. Rev. Lett. **59**, 2806 (1987)
34. R.K. Hayden et al., Phys. Rev. Lett. **66**, 1749 (1991); O.H. Hughes et al., J. Vac. Sci. Technol. **B7**, 1041 (1989)
35. J. Wang et al., Phys. Rev. Lett. **73**, 1146 (1994); P. Beton et al., Phys. Rev. Lett. **75**, 1996 (1995)
36. J.W.L. Sakai et al., Phys. Rev. B **48**, 5664 (1993)
37. M.F. Crommie et al., Nature **262**, 218 (1993)
38. A. Patanè et al., Phys. Rev. B **62**, 13595 (2000)
39. E.E. Vdovin et al., Science **290**, 124 (2000)
40. P.C. Main et al., Phys. Rev. Lett. **84**, 729 (2000)
41. A. Levin et al., Phys. Stat. Sol. **224**, 715 (2001)
42. D. Bimberg et al., *Quantum Dot Heterostructures* (John Wiley & Sons, New York, 1999)
43. O. Stier et al., Phys. Rev. B **59**, 5688 (1999)
44. L.W. Wang et al., Phys. Rev. B **59**, 5678 (1999)
45. Zh.I. Alferov et al., Sov. Phys. Semicond. **4**, 1573 (1970); Zh.I. Alferov et al., Fiz. Tekh. Poluprovodn. **4**, 1826 (1970); I. Hayashi et al., Appl. Phys. Lett. **17**, 109 (1970); R. C. Miller et al., J. Appl. Phys. **47**, 4509 (1976); R.D. Dupuis et al., Appl. Phys. Lett. **32**, 295 (1978); W.T. Tsang, Appl. Phys. Lett. **39**, 786 (1981); Zh.I. Alferov et al., Pis'ma v Zh. Tekhn. Fiz. **14**, 1803 (1988); N. Chand et al., Appl. Phys. Lett. **58**, 1704 (1991); N. Kirstaedter et al., Electron. Lett. **30**, 1416 (1994); N.N. Ledenstov et al., Phys. Rev. B **54**, 8743 (1996); G.T. Liu et al., Electron. Lett. **35**, 1163 (1999); R.L. Sellin et al., Appl. Phys. Lett. **78**, 1207 (2001)
46. D. Bimberg et al., MRS Bulletin July 2002, p. 531
47. R.L. Sellin et al., Appl. Phys. Lett. **78**, 1207 (2001)
48. N. Kirstaedter et al., Electron. Lett. **30**, 1416 (1994)
49. H. Shoji et al., IEEE Photon. Technol. Lett. **7**, 1385 (1995)
50. Z.I. Alferov et al., Semiconductors **30**, 193 (1996)
51. N.N. Ledenstov et al., Phys. Rev. B **54**, 8743 (1996)
52. Q. Xie et al., IEEE Photon. Technol. Lett. **8**, 965 (1996)
53. X. Huang et al., Electron. Lett. **36**, 41 (2001)
54. N. Chand et al., Appl. Phys. Lett. **58**, 1704 (1991)
55. H. Heinrichsdorff et al., Appl. Phys. Lett. **76**, 556 (2000)
56. R.L. Sellin et al., Electron. Lett. **38**, 883 (2002)
57. V.M. Ustinov et al., Tech. Phys. Lett. **24**, 49 (1998)
58. K. Hunzer et al., J. Appl. Phys. **87**, 1496 (2000)
59. G. Park et al., Appl. Phys. Lett. **75**, 3267 (1999)
60. D.L. Huffaker et al., Appl. Phys. Lett. **73**, 2564 (1998)
61. K. Mukai et al., IEEE J. Quantum Electron. **36**, 472 (2000)
62. V.M. Ustinov et al., Appl. Phys. Lett. **74**, 2815 (1999)
63. X. Huang et al., Electron. Lett. **36**, 41 (2000)
64. A.R. Kovsh et al., Electron. Lett. **38**, 1104 (2002)
65. J.W. Jang et al., Appl. Phys. Lett. **85**, 3675 (2004)
66. M.V. Maksimov et al., Semiconductors **38**, 732 (2004)
67. A. Wilk et al., J. Cryst. Growth **278**, 335 (2005)